

This is an Open Access document downloaded from ORCA, Cardiff University's institutional repository: <https://orca.cardiff.ac.uk/id/eprint/122334/>

This is the author's version of a work that was submitted to / accepted for publication.

Citation for final published version:

Li, Jian, Li, Wei, Alves, Tiago M. , Rebesco, Michele, Zhan, Wenhuan, Sun, Jie, Mitchell, Neil C. and Wu, Shiguo 2019. Different origins of seafloor undulations in a submarine canyon system, northern South China Sea, based on their seismic character and relative location. *Marine Geology* 413 , pp. 99-111.
10.1016/j.margeo.2019.04.007

Publishers page: <http://dx.doi.org/10.1016/j.margeo.2019.04.007>

Please note:

Changes made as a result of publishing processes such as copy-editing, formatting and page numbers may not be reflected in this version. For the definitive version of this publication, please refer to the published source. You are advised to consult the publisher's version if you wish to cite this paper.

This version is being made available in accordance with publisher policies. See <http://orca.cf.ac.uk/policies.html> for usage policies. Copyright and moral rights for publications made available in ORCA are retained by the copyright holders.



1 **Different origins of seafloor undulations in a submarine canyon system, northern**
2 **South China Sea, based on their seismic character and relative location**

3 Jian Li^{a, b}, Wei Li^{a, b*}, Tiago M. Alves^c, Michele Rebesco^d, Wenhuan Zhan^{a, b}, Jie Sun^a, Neil C.
4 Mitchell^e, Shiguo Wu^f

5
6 ^aCAS Key Laboratory of Ocean and Marginal Sea Geology, South China Sea Institute of
7 Oceanology, Chinese Academy of Sciences, Guangzhou 510301, P.R. China

8 ^b University of Chinese Academy of Sciences, Beijing 100049, P.R. China

9 ^c 3D Seismic Lab, School of Earth and Ocean Sciences, Cardiff University, Main Building, Park
10 Place, Cardiff, CF10 3AT, United Kingdom

11 ^d Istituto Nazionale di Oceanografia e di Geofisica Sperimentale (OGS), Borgo Grotta Gigante
12 42/C, Sgonico, 34010 Trieste, Italy

13 ^e School of Earth and Environmental Sciences, The University of Manchester, Manchester M13
14 9PL, UK

15 ^f Institute of Deep-sea Science and Engineering, Chinese Academy of Sciences, Sanya 572000, P.R.
16 China

17 *Correspondence to: Dr. Wei Li (wli@scsio.ac.cn)

18

19 **Abstract**

20 High-resolution 2D and 3D seismic data are used to investigate the morphology,
21 internal architecture and origin of widespread seafloor undulations in the eastern area
22 of a submarine canyon system, northern South China Sea. The seafloor undulations
23 reveal similar seafloor morphologies, and three different types (Types A, B and C) can
24 be classified based on their relative locations and internal seismic characters. Types A

25 and B are observed in the canyon areas, whereas Type C occurs in the canyon heads.
26 Seismic reflections within Types A and C are continuous and have an upslope
27 migrating trend, while Type B seafloor undulations are separated by listric faults. Our
28 analysis reveals the origins of these three different types of seafloor undulations. Type
29 A seafloor undulations are sediment waves formed by turbidity currents flowing
30 through the submarine canyons. Gravity-driven submarine creep resulted in the
31 formation of Type B seafloor undulations. Type C undulations are sediment waves
32 generated by internal waves interacting with the continental slope. Our results provide
33 information about the origin of widespread seafloor undulations in other submarine
34 canyon systems. It is also of great significance to future risk assessments, as the study
35 area now is one of the most active regions for hydrocarbon exploration in SE Asia.

36

37 **Keywords:** South China Sea; Submarine canyons; Seafloor undulations; Bathymetry;
38 Internal seismic character.

39

40 **1 Introduction**

41 Seafloor undulations are one of the most widespread bedforms on both passive
42 and active continental margins (Symons et al., 2016), revealing a wide range of
43 morphologies, dimensions and sediment types (Ribó et al., 2018). Seafloor
44 undulations are generated by a combination of depositional and erosional processes,
45 and their crests comprise positive features relative to the surrounding seafloor
46 (Symons et al., 2016). Seafloor undulations have been documented in a wide range of

47 submarine settings, including on continental shelves (Belde et al., 2017), continental
48 slopes (Ribó et al., 2018), continental rises (Gonthier et al., 2002), abyssal plains
49 (Baldwin et al., 2017), the slopes of volcanic islands (Pope et al., 2018), and
50 submarine canyons and channels (Gong et al., 2012). Seafloor undulations are
51 commonly associated with sediment waves and sediment deformation under
52 gravity-driven submarine creep (Wynn and Stow, 2002).

53 Sediment waves can be created by along-slope bottom currents, downslope
54 turbidity currents or by a combination of both their processes (Wynn and Stow, 2002;
55 Symons et al., 2016). Sediment waves formed by bottom currents are chiefly related
56 to sediment drifts, with their wavelength and height reaching up to 10 km and 150 m,
57 respectively (Flood et al., 1993; Wynn and Stow, 2002; Rebesco et al., 2007).
58 Sediment waves formed by turbidity currents are common in channel levees, canyon
59 and channel mouths, and typically reveal wavelengths and heights of up to 7 km and
60 80 m, respectively (Wynn and Stow, 2002). Sediment waves can also be generated by
61 internal waves (Karl et al., 1986; Reeder et al., 2011; Ribó et al., 2016), and have been
62 found in the heads of submarine canyons. Here, they show average wave heights of 5
63 m and wavelengths of up to 650 m (Karl et al., 1986). Sediment waves have been
64 widely documented on the northern South China Sea margin, especially in the
65 Qiongdongnan (Jiang et al., 2013; Chen et al., 2017) and Taixinan Basin (Damuth,
66 1979; Gong et al., 2012; Kuang et al., 2014).

67 Apart from sediment waves formed by depositional and oceanographic processes,
68 seafloor creep can also generate vast fields of undulations where slope gradients and

69 sedimentation rates are relatively high (Lee and Chough, 2001; Faugeres et al., 2002;
70 Rebesco et al., 2009; Shillington et al., 2012; Li et al., 2016a). They can generate
71 waves up to 10 km in length and 100 m in height (Wynn and Stow, 2002). Seafloor
72 creeping can involve into large-scale submarine landslides, posing major geohazards
73 to infrastructure such as telecommunication cables and pipelines (Lee and Chough,
74 2001; Shillington et al., 2012). Therefore, it is of great importance to correctly
75 identify the origin of seafloor undulations, and to understand the tectonic, sedimentary
76 and oceanographic setting in which they occur (Shillington et al., 2012; Belde et al.,
77 2017).

78 A large-scale submarine canyon system, consisting of eighteen regular spaced,
79 linear, sub-parallel submarine canyons, has been previously documented on the
80 continental slope of the Pearl River Mouth Basin (He et al., 2014; Ma et al., 2015; Li
81 et al., 2016b) (Figs. 1 and 2). The study area in this work is situated in the eastern part
82 of this submarine canyon system at water depths between 600 and 1600 m (Fig. 2).
83 Here, seafloor undulations are broadly distributed in the thalwegs, flanks and heads of
84 the studied submarine canyons, and doubts still exist on their origin and formation
85 processes. The seafloor undulations in the heads and flanks of the canyons have been
86 proposed to reflect seafloor creep and landslides (He et al., 2014). However, Qiao et
87 al. (2015) considered that seafloor undulations in the heads of the canyons relate to
88 creep folds induced by soft sediment deformation, while waves in the lower segment
89 of canyons are associated to turbidity currents overflowing their thalwegs.
90 Additionally, seafloor undulations in the heads and on the flanks of canyons are

91 caused by sediment deformation (Li et al., 2016b). Ma et al. (2015) also interpreted
92 seafloor undulations in the heads and flanks of submarine canyons as failure scars.
93 Notwithstanding these differing interpretations, it is of great importance to determine
94 the exact origin and formation processes of these seafloor undulations, and their
95 implications for future geohazard assessments. The study area is now one of the most
96 active deep-water regions for hydrocarbon exploration on the northern South China
97 Sea margin. In this study, a combination of 2D and 3D seismic data, and
98 high-resolution bathymetry derived from 3D seismic data, are used to:

99 (a) investigate the morphology of the seafloor undulations;

100 (b) describe their detailed internal architectures on high-resolution seismic
101 profiles;

102 (c) determine the origin of seafloor undulations in different segments of
103 submarine canyons;

104 (d) discuss the implications of identifying seafloor undulations on continental
105 margins.

106

107 **2 Geological setting**

108 The South China Sea (SCS) is located at the junction between the Pacific, the
109 Indian-Australian, and the Eurasian tectonic plates, being the largest and deepest
110 marginal sea in the western Pacific Ocean (Taylor and Hayes, 1980). Several major
111 sedimentary basins occur along its northern margin, such as the Yinggehai,
112 Qiongdongnan, Pearl River Mouth, and Taixinan Basins (Xie et al., 2006) (Fig.1). As

113 the largest deep-water basin in the northern South China Sea, the Pearl River Mouth
114 Basin is also one of the most important petroliferous regions of China (Dong et al.,
115 2009; Zhu et al., 2009).

116 The Baiyun Sag is an intraslope basin, with a water depth ranging from 200 to
117 2000 m, part of the larger Pearl River Mouth Basin (Zhu et al., 2010). A submarine
118 canyon system consisting of eighteen submarine canyons is the most prominent
119 geomorphologic feature of the Pearl River Mouth Basin (Figs. 1 and 2). This
120 submarine canyon system records four evolutionary phases based on its internal
121 seismic facies and spatial distribution (Ma et al., 2015): (1) small individual channels
122 were initially formed in the middle of the Baiyun Sag (13.8-12.5 Ma); (2) channels
123 were enlarged in a second stage because decreasing sediment input and stable tectonic
124 subsidence in the Baiyun Sag increased the slope angle(12.5-10.5 Ma); (3) channels
125 were broadly distributed and covered the entire Baiyun Sag due to a further decrease
126 in sediment input, with the Dongsha Event later enhancing the flow of gravity
127 currents (10.5-5.5 Ma); (4) channel incision ceased in the northeastern Baiyun Sag,
128 while channels continued to develop in the study area to form modern features (5.5-0
129 Ma). In the study area, submarine canyons migrated unidirectionally to the NE from
130 the middle Miocene to the present day due to the continued action of gravity and
131 bottom currents (Zhu et al., 2010; Gong et al., 2013; Jiang et al., 2017; Gong et al.,
132 2018).

133 Three major water masses exist at different depths on the northern South China
134 Sea (Fig. 1).They comprise seasonal surface water masses (at < 350 m water depth),

135 intermediate water masses (between 350 m and 1350 m water depth), and deep-water
136 masses (at > 1350 m water depth) (Chen and Wang, 1998; Chen, 2005; Zhu et al.,
137 2010; Gong et al., 2013). The study area is mainly affected by intermediate water and
138 deep-water masses. Intermediate water, itself sourced from the North Pacific
139 intermediate water, is considered to have an anti-cyclonic flow that was established in
140 the late Miocene. It is characterised by salinity values between 34.35 and 34.43, with
141 temperature ranging from 7 to 10°C (Chen and Wang, 1998; Chen, 2005; Yang et al.,
142 2010; Chen et al., 2014). Deep-water masses associated with the southwestward flow
143 of the Northern Pacific Deep Water through the Luzon Strait, have a cyclonic
144 circulation. Deep-water circulation was established in the late Miocene and gradually
145 evolved into the modern pattern at ~1.0 Ma (Ludmann et al., 2005; Chen et al., 2014).
146 At present, the velocity of deep-water masses generally varies between 0-2cm/s based
147 on *in situ* observations (Zhao et al., 2015).

148 Internal waves in the northern South China Sea are the largest waves
149 documented in the world's oceans (Zhao et al., 2004; Li et al., 2011; Alford et al.,
150 2015). Active internal wave fields in the northern South China Sea occur in the
151 vicinity of the Dongsha Island and Shenhu Ansha shoal (Fig. 1). Remote sensing
152 studies suggest that internal waves originate either from the local continental shelf
153 break, or from the Luzon Strait on the eastern margin of the South China Sea, as a
154 result of interactions between strong tides and local bathymetric features (Zhao et al.,
155 2004; Li et al., 2008). These internal waves propagate into shallow waters and
156 ultimately dissipate on the continental shelf (Li et al., 2011; Reeder et al., 2011; Ma et

157 al., 2016).

158

159 **3 Data and methods**

160 The dataset used in this study consist of high-resolution bathymetric data derived
161 from 3D seismic and 2D/3D seismic profiles (Figs. 2 and 3). The seismic data were
162 acquired by China National Offshore Oil Corporation using a 3000-m long streamer
163 with 240 channels. The 3D seismic volumes were collected with a sampling interval
164 of 4 ms and processed with a bin spacing of 12.5 m × 25 m in their cross-line and
165 inline directions, respectively. The frequency bandwidth of the seismic data is 30–45
166 Hz, providing an average vertical resolution of 8–10 m for the depth of occurrence of
167 seafloor undulations. The vertical scale for all the seismic profiles used in this study is
168 two-way travel time (TWT). Schlumberger's Geoframe® 4.5 software was used to
169 visualise and interpret the seismic data.

170 The interpreted high-resolution bathymetric data covers the submarine canyon
171 system of the Pearl River Mouth Basin in almost its entirety. Horizontal and vertical
172 resolutions for the bathymetric data are ~100 m and 3–6 m, respectively. This
173 resolution is sufficient to gather information on the dimensions, water depths and
174 orientations of large-scale bedforms on the continental slope (Figs. 2 and 3).

175

176 **4 Results**

177 **4.1 Seafloor morphology**

178 **4.1.1 General geomorphology**

179 High-resolution bathymetric data shows that the continental slope has an
180 inclination of $\sim 2^\circ$ between 300 m and 1600 m water depth (Figs. 2 and 3). The
181 submarine canyons on the continental slope are connected to the wide continental
182 shelf and deep-water basin, and are named in this work, from southwest to northeast,
183 as C1 to C18 (Fig.2). All submarine canyons are roughly perpendicular to the
184 continental slope, and show a NW-SE orientation. Submarine canyons have lengths of
185 15-40 km, widths ranging from 2 to 5 km, and incision depths of 100-350 m (Fig.2).
186 Flanking strata between the submarine canyons become gradually narrower in the
187 downslope direction(Fig.2).

188 The high-resolution bathymetric map shows that the seafloor in the heads and
189 flanks of the westernmost submarine canyons C1 to C8 is relatively smooth compared
190 to the easternmost submarine canyons (C9-C18). The heads of canyons C9 to C18 are
191 rough and characterised by widespread seafloor undulations. In addition, multiple
192 slide scarps are observed in the downslope region of the submarine canyons (Fig. 2).
193 The dimensions of these slide scarps range from hundreds of meters to several
194 kilometres in length, and can be dozens of meters in height (Fig. 2).

195

196 **4.1.2 Morphological description of the seafloor undulations**

197

198 Seafloor undulations are chiefly located in the canyon thalwegs, flanks and heads
199 of Canyons C9 to C18 (Figs. 2 and 3).

200 **(a) Seafloor undulations on the canyon flanks and lower slope**

201 Compared to seafloor undulations at the canyon heads, undulations on the flanks
202 and lower slope are smaller and more complex in plan view (Figs. 2 and 3). It is
203 difficult to trace the crests of the seafloor undulations on the bathymetric map.
204 However, the bathymetric profiles reveal that the wavelength (measured from trough
205 to trough) of seafloor undulations varies from 1 km to 2 km on the canyon flanks and
206 lower slope (Fig. 4). Wave height ranges from 50 m to 100 m. In addition, a series of
207 slide scars are observed on the canyon flanks (Fig. 2).

208

209 **(b) Seafloor undulations in the canyon heads**

210 Multiple seafloor undulations were identified in the heads of the canyons at a
211 water depth between 600 m and 900 m. Their strikes are roughly perpendicular to the
212 canyon axis (Figs. 3 and 5a). The crests of the seafloor undulations (see red lines in
213 Fig 3b), are generally parallel or sub-parallel to the bathymetric contours. In addition,
214 the crests of the seafloor undulations show no clear bifurcation in plan view.
215 Topographic profiles crossing the head of the canyons reveal a variety of dimensions
216 with wavelength ranging from 0.8 km to 1.5 km (Fig. 5). Wave height ranges from 20
217 m to 50 m.

218

219 **4.2 Seismic characteristics of the seafloor undulations**

220 Several high-resolution seismic profiles crossing the thalwegs, flanks and heads
221 of the submarine canyon system image the internal architecture of the seafloor
222 undulations (Fig. 2). The seafloor undulations can therefore be divided into three main

223 types, A, B and C, based on their internal architecture and relative locations in the
224 submarine canyon system.

225

226 **4.2.1 Type A seafloor undulations**

227 Type A undulations are observed in the lower segments of the canyon thalwegs
228 (Figs. 3, 6 and 7). The sedimentary succession affected by the undulations has a
229 thickness of ~200 ms TWT (Fig.7). Seismic profiles show that most seismic
230 reflections are continuous, and can be traced from one wave to the next (Figs. 6 and 7).
231 However, multiple mass-transport deposits (MTDs), characterised by discontinuous
232 and chaotic internal seismic reflections, are also observed, proving that important
233 sediment instability has occurred in the lower segment of the canyon thalwegs (Fig.7).

234 Discrete undulations reveal an asymmetric morphology with gentle upslope
235 flanks and steep downslope flanks (Fig. 7). They are commonly thicker on their
236 upslope flanks. Undulations show a marked trend for upslope migration (Fig.7b).
237 Deeply buried undulations show relatively shorter upslope flanks and longer
238 downslope flanks (Fig. 7). In contrast, the upslope flanks of shallow-buried
239 undulations are longer than their downslope counterparts (Fig. 7). Downslope flanks
240 also reveal erosional truncations in shallow-buried undulations (Fig. 7).

241

242 **4.2.2 Type B seafloor undulations**

243 Type B undulations occur on the canyon flanks, further upslope when compared
244 to Type A. High-resolution seismic lines crossing the canyon flank between C11 and

245 C12 reveal the internal architecture of Type B undulations (Figs. 2, 6, 8 and 9). The
246 sedimentary succession affected by these undulations has a thickness of ~200 ms
247 TWT. A series of high-amplitude (enhanced) seismic reflections can be identified
248 along the base of the undulations (Figs. 6, 8 and 9a). They are usually distributed
249 around, or above, focused fluid-flow structures such as gas chimneys (Figs. 8 and 9a).

250 Seismic reflections in Type B undulations are not continuous and cannot be
251 traced across the troughs separating distinct sediment waves. Most of these
252 undulations are separated by listric faults (Figs. 6, 8 and 9). The troughs of the
253 undulations are related to displacements of ~100ms TWT along the fault planes (Fig.
254 9).

255 Type B undulations are characterised by their asymmetric morphology (Fig. 9).
256 Upslope flanks reveal sub-parallel seismic reflections, whereas their downslope flanks
257 are thin and show erosional truncation within shallow undulations (Fig. 9). The crests
258 of Type B undulations also show an apparent upslope migration trend.

259

260 **4.2.3 Type C seafloor undulations**

261 Type C undulations are observed close to the heads of the canyons. The thickness
262 of the strata affected by Type C undulations decreases from ~200 ms TWT to ~100 ms
263 TWT in a downslope direction (Figs. 6, 10 and 11). Type C undulations are
264 characterised by their wavy, asymmetric morphology and laterally continuous seismic
265 reflections, although chaotic seismic reflections can also be identified due to the
266 presence of MTDs (Fig. 11b). The upslope flanks of the undulations are characterised

267 by aggradation, whereas their downslope flanks are dominated by erosion and
268 non-deposition. Thus, the crests of Type C undulations reveal an upslope migration
269 trend with time. Note that some of shallow buried undulations reveal erosional
270 truncation on their downslope flanks (Fig. 10a).

271

272 **5 Discussion**

273

274 **5.1 Genesis of widespread seafloor undulations in a submarine canyon system**

275

276 Seafloor undulations have been observed in submarine canyon systems all
277 around the world (Gonthier et al., 2002; Gong et al., 2012; Ribó et al., 2018). Four
278 main hypotheses have been proposed for their genesis based on the environment
279 settings in which seafloor undulations occur, their morphological characteristics, and
280 internal architectures. These four hypotheses include: (1) bottom currents (Masson et
281 al., 2002; Baldwin et al., 2017; Belde et al., 2017); (2) turbidity currents (Lewis and
282 Pantin, 2002; Normark et al., 2002; McCave, 2017); (3) internal waves (Karl et al.,
283 1986; Droghei et al., 2016; Ma et al., 2016; Ribó et al., 2016); and (4) gravity-driven
284 downslope submarine creeps (Lee and Chough, 2001; Shillington et al., 2012; Li, et
285 al., 2016a). In the following sections, the formation mechanisms of seafloor
286 undulations are discussed for the study area based on the criteria proposed by Wynn
287 and Stow (2002) and Symons et al. (2016).

288

289 **5.1.1 Origin and formation process of Type A seafloor undulations(canyon**
290 **thalwegs)**

291

292 Turbidity currents are major downslope sediment transport processes, and are
293 commonly identified in submarine canyons, channels and gullies (Shepard, 1981;
294 Parker, 1982; Canals et al., 2006; Talling et al., 2015; Paull et al., 2018). Sediment
295 waves generated by turbidity currents have been documented in regions such as the
296 Monterey Fan channel (Normark et al., 1980), on the South Iberian Margin (Alves et
297 al., 2003; Perez-Hernandez et al., 2014) and in the northern South China Sea (Gong et
298 al., 2012; Jiang et al., 2013).

299 In the study area, Type A undulations are closely linked to the lower segments of
300 the canyon thalwegs (Figs. 26 and 7). Internal seismic reflections within the
301 undulations are continuous and can be traced from one wave to the next (Figs. 6 and
302 7). Each undulation reveals an asymmetric morphology, with gentle upslope flanks
303 and steep downslope flanks (Fig. 7). All these undulations show a significant trend of
304 upslope migration as their upslope flanks accumulate sediment more rapidly than their
305 downslope flanks (Fig. 7). Based on criteria proposed by Wynn and Stow (2002),
306 Type A undulations are similar to sediment waves generated by turbidity currents, e.g.
307 the Selvagens sediment-wave field, NE Atlantic (Wynn et al., 2000), and the
308 Hikurangi Trough east of New Zealand (Lewis and Pantin, 2002).

309 Our study area is located on the continental slope of the northern South China
310 Sea. In this region, multiple submarine instability features, i.e. creeps, slumps and

311 landslide complexes, are developed in an area incised by multiple submarine canyons
312 (He et al., 2014; Chen et al., 2016). Previous studies suggest that turbidity currents are
313 produced by the downslope transport of slumps and mass flows (Parker, 1982; Ercilla
314 et al., 2002). Li et al. (2015) also suggest that slumps and mass flows occurred
315 frequently in the past to generate turbidity currents in submarine canyon systems of
316 the northern South China Sea margin. As discussed above, we infer that Type A
317 undulations comprise sediment waves produced by turbidity currents associated with
318 frequent slumping and mass wasting in the submarine canyons.

319

320 **5.1.2 Origin and formation processes of Type B seafloor undulations (canyon** 321 **flanks)**

322

323 The internal seismic reflections within Type B undulations are not continuous,
324 and cannot be traced across successive troughs separating the observed undulations
325 (Figs. 6, 8 and 9). These troughs are commonly associated with listric faults (Figs. 6,
326 8 and 9). Undulations are generally thicker on their upslope flanks, and thinner (or
327 even eroded) in their downslope flanks (Fig. 9). Seafloor undulations associated with
328 listric faults have been documented by Faugères et al. (2002) and Gonthier et al.
329 (2002). They were interpreted as reflecting gravity-driven downslope submarine creep.
330 The basic conditions for the formation of submarine creeps have been summarised by
331 Hill et al. (1982), including the presence of faulting and glide planes. When
332 deforming the sediments, a basal décollement zone is formed at the lower boundary of

333 the strata. Listric faults act as glide planes for the displacement of the layered
334 sediment. The regional slope gradient of submarine canyon systems varies from 1.5°
335 to 2.5°, being ~1.6° on average (He et al., 2014; Li et al., 2016b).

336 In the study area, Type B undulations are mainly located on the canyon flanks,
337 where slope gradients are steep (up to 8 degrees). Sediment drilled on the flanks of the
338 submarine canyons' lower segments consists of massive silty mud and a few sandy to
339 silty intervals with weak layers (Qiao et al., 2015). Here, soft sediment deformation
340 (submarine creep) is likely controlled by the slope gradient and strength of the
341 sediment (Wynn and Stow, 2002). Due to progressing gravity-driven downslope
342 deformation, the local accumulating of strain resulted in the development of local
343 faults within sediment waves (Liet al., 2016a). Listric faults are developed within
344 troughs, leading to significant displacement of adjacent undulations (Fig 9). Thus, we
345 interpret Type B undulations as the result of soft sediment deformation produced by
346 gravity-driven downslope submarine creep.

347 Additionally, gas chimneys, pipes, large-scale normal faults and shallow gas are
348 widespread on the lower slope of the interpreted submarine canyon system (Sun et al.,
349 2012; Chen et al., 2016). Abundant acoustic anomalies, revealed as high-amplitude
350 (enhanced) seismic reflections, can be observed close to the lower boundary of Type
351 B undulations (Figs. 6, 8 and 9a). Elsewhere, similar enhanced seismic reflections
352 have been associated with free gas and fluid accumulated in shallow strata (e.g. Sun et
353 al., 2012; 2017). Gas chimneys, pipes and faults can act as pathways for the vertical
354 migration of free gas and fluids (Sun et al., 2017). The presence of free gas and fluid

355 increases overpressure in shallow strata, and reduces its shear strength until the
356 creeping movements occur (e.g. Sultan et al., 2004; Urlaub et al., 2018).

357

358 **5.1.3 Origin and formation process of the Type C seafloor undulations (canyon** 359 **heads)**

360 Type C undulations are identified in the canyon head areas (Figs. 3, 6, 10 and 11).
361 The origin of these undulations has been interpreted in He et al. (2014), Qiao et al.
362 (2015), Ma et al. (2015), and Li et al. (2016b). Some of these authors have suggested
363 that seafloor undulations were generated by submarine soft-sediment deformation due
364 to slow gravity-driven downslope creeping (He et al., 2014; Qiao et al., 2015). Others
365 have stressed their association with failure scars and fissures (Ma et al., 2015; Li et al.,
366 2016b). Obviously, debate still exists about the origin and formation processes of
367 Type C undulations.

368 The internal seismic reflections of Type C undulations can be traced across the
369 crests and troughs of each wave in the canyon heads (Figs. 6, 10 and 11). Such an
370 internal seismic architecture suggests a depositional origin for Type C undulations,
371 rather than creeping and faulting. These undulations are similar to sediment waves
372 formed by turbidity currents on continental margins (Wynn and Stow, 2002). However,
373 the study area is located on the upper continental slope and is connected to a wide
374 continental shelf (Fig. 1). Type C undulations are widespread in the canyon heads, but
375 there is no major sediment source nearby, capable of producing unconfined turbidity
376 flows. For this reason, we consider unlikely Type C seafloor undulations to be

377 generated by turbidity currents.

378 Previous studies have considered bottom currents as an important process
379 forming sediment waves, such as in parts of the northeast Rockall Trough (Masson et
380 al., 2002), the Caroline Basin in the West Pacific Ocean (Baldwin et al., 2017), and
381 even in lakes (Ceramicola et al., 2001). Bottom currents, which are associated with
382 the North Pacific intermediate water, affect the northern South China Sea at a water
383 depth of 350-1350 m (Chen and Wang, 1998; Chen, 2005; Zhu et al., 2010; Chen et
384 al., 2014). Bottom currents flow to the northeast along the continental slope and affect
385 sedimentation in the studied submarine canyon system (Zhu et al., 2010; Gong et al.,
386 2013; Jiang et al., 2017). Sediment waves formed by bottom currents are normally
387 oblique to the continental slope, and their crests are aligned perpendicularly or
388 obliquely to bottom current flows (Wynn and Stow, 2002). The crests of these
389 sediment waves are also straight or slightly sinuous, such as this of sediment waves at
390 the toe of the South China Sea continental slope, southwest Taiwan (Gong et al.,
391 2012). In contrast with the latter geometries, the crests of Type C undulations are
392 characterised by their curved shape in plan view, and are generally parallel or
393 sub-parallel to the bathymetric contours (Figs. 2 and 3). We thus consider unlikely
394 that bottom currents are responsible for the Type C undulations.

395 In recent years, an increasingly larger number of studies have considered internal
396 waves as a formation mechanism for the generation of seafloor sediment waves (Karl
397 et al., 1986; Reeder et al., 2011; Ribó et al., 2016). In fact, the South China Sea hosts
398 the largest internal waves observed in the world's oceans (Li et al., 2011; Alford et al.,

399 2015) (Fig. 1). They are the result of the interaction between strong tidal currents and
400 the abrupt local bathymetry (Zhao et al., 2004; Li et al., 2008). Several fields of
401 sediment wave have been reported on the continental shelf and slope off the Dongsha
402 Islands, and they were interpreted as generated by internal waves interacting with the
403 continental margin (Reeder et al., 2011; Ma et al., 2016). Our study area is just located
404 on the western continental slope of the Dongsha Islands (Fig. 1), where internal waves
405 have been documented by Ma et al. (2016). This indicates that the seafloor undulations
406 in the canyon head areas might be produced by internal waves.

407 The breaking of internal waves on slope surfaces can create intense turbulence
408 near the seafloor, generating local bottom currents with sufficient strength to
409 resuspend and transport sediment (Bogucki and Redekopp, 1999; Ribbe and Holloway,
410 2001; Reeder et al., 2011). Moreover, internal waves' energy may be amplified at the
411 canyon heads, as documented in the Hudson Canyon on the US Atlantic margin
412 (Hotchkiss and Wunsch, 1982), and the Navarinsky Canyon in the Bering Sea (Karl et
413 al., 1986). Consequently, when internal waves interact with the heads of the
414 submarine canyons, they can become unstable, break and transfer wave energy to
415 generate intense turbulence near the seafloor (Reeder et al., 2011; Pomar et al., 2012;
416 Ribóet al., 2016). These seafloor-fluid mixtures, under the action of gravity, move
417 downslope (Hotchkiss and Wunsch, 1982; Karl et al., 1986; Pomar et al., 2012).

418 A recent study by Ma et al. (2016) indicates that two types of sand waves can be
419 discerned near the shelf break of the northern South China Sea. The crests of sand
420 waves generated by internal tides are parallel to the isobaths, and are similar to the

421 crests in the canyon heads of our study area (Fig. 3b). A primary question about the
422 observed internal waves is how were they generated. Two sources of internal waves
423 have been observed in the northern South China Sea. Based on remote sensing images,
424 internal waves have been related to tidal action and Kuroshio current flow over the
425 Luzon Strait on the eastern margin of the South China Sea (Zhao et al., 2004; Li et al.,
426 2008). The other source of internal waves in the South China Sea is associated to the
427 shelf break, which records incident trans-basin waves and internal tides (Guo et al.,
428 2012; Reeder et al., 2011).

429 We infer that the Type C undulations identified in this work are most likely
430 generated by internal waves. The source of these internal waves cannot be confirmed
431 due to the lack of field measurements. In addition, when internal tides propagate, their
432 energy dissipates because of inherent mixing processes in the ocean, accompanied by
433 the generation of internal solitary waves (Guo et al., 2012). Therefore, more work is
434 needed (e.g. *in situ* measurements and numerical simulations) to determine the source
435 of the internal waves affecting the canyon head areas.

436

437 **5.2. Significance of widespread seafloor undulations to geohazard assessments in** 438 **the Pearl River Mouth Basin**

439

440 The formation of seafloor undulations has been attributed to a variety of
441 sedimentary, tectonic, and gravitational processes (Cartigny et al., 2011; Shillington et
442 al., 2012). It is of great significance to correctly pinpoint the origin of seafloor

443 undulations as they are essential for understanding the oceanographic, sedimentary,
444 and tectonic evolution of basins and margins and, particularly, for assessing
445 geohazards related to slope instability (Shillington et al., 2012). The Pearl River
446 Mouth Basin is one of the most important hydrocarbon-rich basins in the northern
447 South China Sea and has been the focus of hydrocarbon expeditions and academic
448 drilling (ODP Site 1148, IODP Expedition 349) for the past two decades (Li et al.,
449 2005; Li et al., 2014). The submarine canyon area is also a target area for gas-hydrate
450 exploration, e.g. the Shenhu area between Canyons C9 and C11 (Guan and Liang,
451 2018).

452 In this study, three different types of seafloor undulations (Types A, B and C)
453 (Fig. 12) have been identified in the submarine canyons. These seafloor undulations
454 show very similar morphologies on the bathymetric maps in Figs. 2 and 3. However,
455 the internal architectures of these undulations are markedly different. Internal seismic
456 reflections within Types A and C undulations are continuous and all show an apparent
457 upslope migrating pattern (Figs. 7,10 and 11). Types A and C sediment waves are
458 purely generated by sedimentary processes (turbidity currents and internal waves).
459 They are interpreted as the result of turbidity currents flowing within submarine
460 canyons and internal waves interacting with the continental slope, respectively.
461 However, their downslope flanks are quite steep (reaching 8 degrees) and show
462 lengths of up to 700m. As such, the downslope flanks can be preferential areas for
463 slope instability. Type B undulations are the seafloor manifestations of gravity-driven
464 submarine creeping, and resemble the creep folds documented by Shillington et al.

465 (2012) and Li et al. (2016a). They are commonly associated with listric faults, which
466 act as potential glide planes for future slope instability (e.g. Li et al., 2016a).
467 Resulting submarine landslides can pose catastrophic risks to oil and gas exploration
468 and development (e.g. Piper et al., 1999). Therefore, more studies are required to
469 determine the exact distribution of Type B seafloor undulations in the multiple
470 submarine canyon systems of the northern South China Sea.

471

472 **6 Conclusions**

473 High-resolution 2D and 3D seismic data allowed us to investigate the morphology,
474 internal architecture and origin of widespread seafloor undulations in the eastern area
475 of a submarine canyon system, northern South China Sea. The main conclusions of
476 this work are as follows:

477

478 (1) Seafloor undulations are distributed through canyon flanks, thalwegs and
479 canyon-head areas. These seafloor undulations on the canyon flanks and thalwegs
480 have wavelengths up to 2 km and heights up to 100 m. The wavelengths and wave
481 heights on the canyon head areas are up to 1.5 km and 50m, respectively.

482 (2) All identified undulations have similar morphologies on bathymetric maps,
483 but the three different types of seafloor undulations (Types A, B and C) can be
484 determined based on their relative locations and internal characters. Type A
485 undulations occur mainly in the canyon thalwegs, and their internal seismic
486 reflections are continuous, showing an apparent upslope migrating trend. Seismic

487 reflections within Type B undulations are not continuous, but separated by listric
488 faults. Type C undulations are observed in the canyon heads and their crests are
489 roughly parallel to the local bathymetry.

490 (3) Types A and C undulations are sediment waves purely generated by
491 sedimentary processes. Type A sediment waves are formed by turbidity currents
492 flowing through the submarine canyons. Type C sediment waves most likely result
493 from internal waves, which are amplified in the canyon heads, interacting with the
494 continental slope. Type B undulations result from the gravity-driven (downslope)
495 submarine creeping.

496 (4) To correctly identify the origin, formation processes and distribution of
497 sediment waves in the submarine canyon systems off South China will be of great
498 significance for future geohazard assessments in what is a hydrocarbon-rich basin of
499 the South China Sea.

500

501 **Acknowledgements**

502 We thank China National Offshore Oil Corporation for their permission to release
503 the seismic data. This work was financially supported by the National Scientific
504 Foundation of China (Grant No. 41876054) and the Key Laboratory of Ocean and
505 Marginal Sea Geology, Chinese Academy of Sciences (Grant No. OMG18-09). We
506 thank Prof. Puig Pere and Prof. Mike Blum for valuable discussion. Dr. Wei Li is
507 funded by the CAS Pioneer Hundred Talents Program. This paper benefited from the
508 constructive comments of the editor (Prof. Shu Gao), Dr. Chenglin Gong and two

509 anonymous reviewers.

510

511 **References**

- 512 Alford, M.H., Peacock, T., MacKinnon, J.A., Nash, J.D., Buijsman, M.C., Centuroni,
513 L.R., Chao, S.-Y., Chang, M.-H., Farmer, D.M., Fringer, O.B., Fu, K.-H.,
514 Gallacher, P.C., Graber, H.C., Helfrich, K.R., Jachec, S.M., Jackson, C.R.,
515 Klymak, J.M., Ko, D.S., Jan, S., Johnston, T.M.S., Legg, S., Lee, I.H., Lien,
516 R.-C., Mercier, M.J., Moum, J.N., Musgrave, R., Park, J.-H., Pickering, A.I.,
517 Pinkel, R., Rainville, L., Ramp, S.R., Rudnick, D.L., Sarkar, S., Scotti, A.,
518 Simmons, H.L., St Laurent, L.C., Venayagamoorthy, S.K., Wang, Y.-H., Wang, J.,
519 Yang, Y.J., Paluszkiwicz, T., Tang, T.-Y., 2015. The formation and fate of
520 internal waves in the South China Sea. *Nature* 521, 65-U381.
- 521 Alves, T.M., Gawthorpe, R.L., Hunt, D.W., Monteiro, J.H., 2003. Cenozoic
522 tectono-sedimentary evolution of the western Iberian margin. *Marine Geology*
523 195, 75-108.
- 524 Baldwin, K.E., Mountain, G.S., Rosenthal, Y., 2017. Sediment waves in the Caroline
525 Basin suggest evidence for Miocene shifts in bottom water flow in the western
526 equatorial Pacific. *Marine Geology* 393, 194-202.
- 527 Belde, J., Reuning, L., Back, S., 2017. Bottom currents and sediment waves on a
528 shallow carbonate shelf, Northern Carnarvon Basin, Australia. *Continental Shelf*
529 *Research* 138, 142-153.
- 530 Bogucki, D.J., Redekopp, L.G., 1999. A mechanism for sediment resuspension by

531 internal solitary waves. *Geophysical Research Letters* 26, 1317-1320.

532 Canals, M., Puig, P., de Madron, X.D., Heussner, S., Palanques, A., Fabres, J., 2006.

533 Flushing submarine canyons. *Nature* 444, 354-357.

534 Cartigny, M.J.B., Postma, G., van den Berg, J.H., Mastbergen, D.R., 2011. A

535 comparative study of sediment waves and cyclic steps based on geometries,

536 internal structures and numerical modeling. *Marine Geology* 280, 40-56.

537 Ceramicola, S., Rebesco, M., De Batist, M., Khlystov, O., 2001. Seismic evidence of

538 small-scale lacustrine drifts in Lake Baikal (Russia). *Marine Geophysical*

539 *Researches* 22, 445-464.

540 Chen, C.T.A., 2005. Tracing tropical and intermediate waters from the South China

541 Sea to the Okinawa Trough and beyond. *Journal of Geophysical*

542 *Research-Oceans* 110, C05012.

543 Chen, C.T.A., Wang, S.L., 1998. Influence of intermediate water in the western

544 Okinawa Trough by the outflow from the South China Sea. *Journal of*

545 *Geophysical Research-Oceans* 103, 12683-12688.

546 Chen, D.X., Wang, X.J., Völker, D., Wu, S.G., Wang, L., Li, W., Li, Q.P., Zhu, Z.Y.,

547 Li, C.L., Qin, Z.L., Sun, Q.L., 2016. Three dimensional seismic studies of

548 deep-water hazard-related features on the northern slope of South China Sea.

549 *Marine and Petroleum Geology* 77, 1125-1139.

550 Chen, H., Xie, X.N., Van Rooij, D., Vandorpe, T., Su, M., Wang, D.X., 2014.

551 Depositional characteristics and processes of alongslope currents related to a

552 seamount on the northwestern margin of the Northwest Sub-Basin, South China

553 Sea. Marine Geology 355, 36-53.

554 Chen, H.J., Zhan, W.H., Li, L.Q., Wen, M.M., 2017. Occurrence of submarine
555 canyons, sediment waves and mass movements along the northern continental
556 slope of the South China Sea. *Journal of Earth System Science* 126, 73.

557 Damuth, J.E., 1979. Migrating sediment waves created by turbidity currents in the
558 northern South China Basin. *Geology* 7, 520-523.

559 Dong, D.D., Zhang, G.C., Zhong, K., Yuan, S.Q., Wu, S.G., 2009. Tectonic Evolution
560 and Dynamics of Deepwater Area of Pearl River Mouth Basin, Northern South
561 China Sea. *Journal of Earth Science* 20, 147-159.

562 Droghei, R., Falcini, F., Casalbore, D., Martorelli, E., Mosetti, R., Sannino, G.,
563 Santoleri, R., Chiocci, F.L., 2016. The role of Internal Solitary Waves on
564 deep-water sedimentary processes: the case of up-slope migrating sediment
565 waves off the Messina Strait. *Scientific Reports* 6.
566 <https://doi.org/10.1038/srep36376>.

567 Ercilla, G., Wynn, R.B., Alonso, B., Baraza, J., 2002. Initiation and evolution of
568 turbidity current sediment waves in the Magdalena turbidite system. *Marine*
569 *Geology* 192, 153-169.

570 Faugères, J.C., Gonthier, E., Mulder, T., Kenyon, N., Cirac, P., Griboulard, R., Berne,
571 S., Lesuave, R., 2002. Multi-process generated sediment waves on the Landes
572 Plateau (Bay of Biscay, North Atlantic). *Marine Geology* 182, 279-302.

573 Flood, R.D., Shor, A.N., Manley, P.L., 1993. Morphology of abyssal mudwaves at
574 Project MUDWAVES sites in the Argentine Basin. *Deep-Sea Research Part*

575 i-Topical Studies in Oceanography 40, 859-888.

576 Gong, C.L., Wang, Y.M., Peng, X.C., Li, W.G., Qiu, Y., Xu, S., 2012. Sediment waves
577 on the South China Sea Slope off southwestern Taiwan: Implications for the
578 intrusion of the Northern Pacific Deep Water into the South China Sea. *Marine
579 and Petroleum Geology* 32, 95-109.

580 Gong, C.L., Wang, Y.M., Rebesco, M., Salon, S., Steel, R.J., 2018. How do turbidity
581 flows interact with contour currents in unidirectionally migrating deep-water
582 channels? *Geology* 46, 551-554.

583 Gong, C.L., Wang, Y.M., Zhu, W.L., Li, W.G., Xu, Q., 2013. Upper Miocene to
584 Quaternary unidirectionally migrating deep-water channels in the Pearl River
585 Mouth Basin, northern South China Sea. *Aapg Bulletin* 97, 285-308.

586 Gonthier, E., Faugères, J.C., Gervais, A., Ercilla, G., Alonso, B., Baraza, J., 2002.
587 Quaternary sedimentation and origin of the Orinoco sediment-wave field on the
588 Demerara continental rise (NE margin of South America). *Marine Geology* 192,
589 189-214.

590 Guan, J.A., Liang, D.Q., 2018. Discussion on the rapid formation mechanism and
591 evolution process of methane hydrate-bearing sediments in Shenhu Area of
592 northern South China Sea. *Marine and Petroleum Geology* 91, 225-235.

593 Guo, P., Fang, W.D., Liu, C.J., Qiu, F.W., 2012. Seasonal characteristics of internal
594 tides on the continental shelf in the northern South China Sea. *Journal of
595 Geophysical Research-Oceans* 117, C04023.

596 He, Y., Zhong, G.F., Wang, L.L., Kuang, Z.G., 2014. Characteristics and occurrence

597 of submarine canyon-associated landslides in the middle of the northern
598 continental slope, South China Sea. *Marine and Petroleum Geology* 57, 546-560.

599 Hill, P.R., Moran, K.M., Blasco, S.M., 1982. Creep deformation of slope sediments in
600 the Canadian Beaufort Sea. *Geo-Marine Letters* 2, 163-170.

601 Hotchkiss, F.S., Wunsch, C., 1982. Internal waves in Hudson Canyon with possible
602 geological implications. *Deep Sea Research Part A. Oceanographic Research*
603 *Papers* 29, 415-442.

604 Jiang, J., Shi, H.S., Lin, C.S., Zhang, Z.T., Wei, A., Zhang, B., Shu, L.F., Tian, H.X.,
605 Tao, Z., Liu, H.Y., 2017. Sequence architecture and depositional evolution of the
606 Late Miocene to quaternary northeastern shelf margin of the South China Sea.
607 *Marine and Petroleum Geology* 81, 79-97.

608 Jiang, T., Xie, X.N., Wang, Z.F., Li, X.S., Zhang, Y.Z., Sun, H., 2013. Seismic
609 features and origin of sediment waves in the Qiongdongnan Basin, northern
610 South China Sea. *Marine Geophysical Research* 34, 281-294.

611 Karl, H.A., Cacchione, D.A., Carlson, P.R., 1986. Internal-wave currents as a
612 mechanism to account for large sand waves in Navarinsky Canyon head, Bering
613 Sea. *Journal of Sedimentary Petrology* 56, 706-714.

614 Kuang, Z.G., Zhong, G.F., Wang, L.L., Guo, Y.Q., 2014. Channel-related sediment
615 waves on the eastern slope offshore Dongsha Islands, northern South China Sea.
616 *Journal of Asian Earth Sciences* 79, 540-551.

617 Lee, S.H., Chough, S.K., 2001. High-resolution (2-7 kHz) acoustic and geometric
618 characters of submarine creep deposits in the South Korea Plateau, East Sea.

619 Sedimentology 48, 629-644.

620 Lewis, K.B., Pantin, H.M., 2002. Channel-axis, overbank and drift sediment waves in
621 the southern Hikurangi Trough, New Zealand. *Marine Geology* 192, 123-151.

622 Li, C.F., Xu, X., Lin, J., Sun, Z., Zhu, J., Yao, Y.J., Zhao, X.X., Liu, Q.S., Kulhanek,
623 D.K., Wang, J., Song, T.R., Zhao, J.F., Qiu, N., Guan, Y.X., Zhou, Z.Y., Williams,
624 T., Bao, R., Briais, A., Brown, E.A., Chen, Y.F., Clift, P.D., Colwell, F.S., Dadd,
625 K.A., Ding, W.W., Almeida, I.H., Huang, X.L., Hyun, S., Jiang, T., Koppers,
626 A.A.P., Li, Q.Y., Liu, C.L., Liu, Z.F., Nagai, R.H., Peleo-Alampay, A., Su, X.,
627 Tejada, M.L.G., Trinh, H.S., Yeh, Y.C., Zhang, C.L., Zhang, F., Zhang, G.L.,
628 2014. Ages and magnetic structures of the South China Sea constrained by deep
629 tow magnetic surveys and IODP Expedition 349. *Geochemistry, Geophysics,
630 Geosystems* 15, 4958-4983.

631 Li, D., Chen, X., Liu, A., 2011. On the generation and evolution of internal solitary
632 waves in the northwestern South China Sea. *Ocean Modelling* 40, 105-119.

633 Li, Q.Y., Jian, Z.M., Su, X., 2005. Late Oligocene rapid transformations in the South
634 China Sea. *Marine Micropaleontology* 54, 5-25.

635 Li, W., Alves, T.M., Wu, S.G., Rebesco, M., Zhao, F., Mi, L.J., Ma, B.J., 2016a. A
636 giant, submarine creep zone as a precursor of large-scale slope instability
637 offshore the Dongsha Islands (South China Sea). *Earth and Planetary Science
638 Letters* 451, 272-284.

639 Li, X.F., Zhao, Z.X., Pichel, W.G., 2008. Internal solitary waves in the northwestern
640 South China Sea inferred from satellite images. *Geophysical Research Letters* 35.

641 <https://doi.org/10.1029/2008GL034272>.

642 Li, X.S., Liu, L.J., Li, J.G., Gao, S., Zhou, Q.J., Su, T.Y., 2015. Mass movements in
643 small canyons in the northeast of Baiyun deepwater area, north of the South
644 China Sea. *Acta Oceanologica Sinica* 34, 35-42.

645 Li, X.S., Zhou, Q.J., Su, T.Y., Liu, L.J., Gao, S., Zhou, S.W., 2016b. Slope-confined
646 submarine canyons in the Baiyun deep-water area, northern South China Sea:
647 variation in their modern morphology. *Marine Geophysical Research* 37, 95-112.

648 Ludmann, T., Wong, H.K., Berglar, K., 2005. Upward flow of North Pacific Deep
649 Water in the northern South China Sea as deduced from the occurrence of drift
650 sediments. *Geophysical Research Letters* 32, L05614.

651 Ma, B.J., Wu, S.G., Sun, Q.L., Mi, L.J., Wang, Z.Z., Tian, J., 2015. The late Cenozoic
652 deep-water channel system in the Baiyun Sag, Pearl River Mouth Basin:
653 Development and tectonic effects. *Deep Sea Research Part II: Topical Studies in*
654 *Oceanography* 122, 226-239.

655 Ma, X.C., Yan, J., Hou, Y.J., Lin, F.L., Zheng, X.F., 2016. Footprints of obliquely
656 incident internal solitary waves and internal tides near the shelf break in the
657 northern South China Sea. *Journal of Geophysical Research-Oceans* 121,
658 8706-8719.

659 Masson, D.G., Howe, J.A., Stoker, M.S., 2002. Bottom-current sediment waves,
660 sediment drifts and contourites in the northern Rockall Trough. *Marine Geology*
661 192, 215-237.

662 McCave, I.N., 2017. Formation of sediment waves by turbidity currents and

663 geostrophic flows: A discussion. *Marine Geology* 390, 89-93.

664 Normark, W.R., Hess, G.R., Stow, D.A.V., Bowen, A.J., 1980. Sediment waves on the
665 monterey fan levee: A preliminary physical interpretation. *Marine Geology* 37,
666 1-18.

667 Normark, W.R., Piper, D.J.W., Posamentier, H., Pirmez, C., Migeon, S., 2002.
668 Variability in form and growth of sediment waves on turbidite channel levees.
669 *Marine Geology* 192, 23-58.

670 Parker, G., 1982. Conditions for the ignition of catastrophically erosive turbidity
671 currents. *Marine Geology* 46, 307-327.

672 Paull, C.K., Talling, P.J., Maier, K.L., Parsons, D., Xu, J.P., Caress, D.W., Gwiazda,
673 R., Lundsten, E.M., Anderson, K., Barry, J.P., Chaffey, M., O'Reilly, T.,
674 Rosenberger, K.J., Gales, J.A., Kieft, B., McGann, M., Simmons, S.M., McCann,
675 M., Sumner, E.J., Clare, M.A., Cartigny, M.J., 2018. Powerful turbidity currents
676 driven by dense basal layers. *Nature Communications* 9, Article number: 4114.

677 Perez-Hernandez, S., Comas, M.C., Escutia, C., 2014. Morphology of turbidite
678 systems within an active continental margin (the Palomares Margin, western
679 Mediterranean). *Geomorphology* 219, 10-26.

680 Piper, D.J.W., Cochonat, P., Morrison, M., 1999. The sequence of events around the
681 epicentre of the 1929 grand banks earthquake: initiation of debris flows and
682 turbidity currents inferred from sidescan sonar. *Sedimentology* 46, 79–97.

683 Pomar, L., Morsilli, M., Hallock, P., Bádenas, B., 2012. Internal waves, an
684 under-explored source of turbulence events in the sedimentary record.

685 Earth-Science Reviews 111, 56-81.

686 Pope, E.L., Jutzeler, M., Cartigny, M.J.B., Shreeve, J., Tailing, P.J., Wright, I.C.,
687 Wysoczanski, R.J., 2018. Origin of spectacular fields of submarine sediment
688 waves around volcanic islands. *Earth and Planetary Science Letters* 493, 12-24.

689 Qiao, S.H., Su, M., Kuang, Z.G., Yang, R., Liang, J.Q., Wu, N.Y., 2015.
690 Canyon-related undulation structures in the Shenhu area, northern South China
691 Sea. *Marine Geophysical Research* 36, 243-252.

692 Rebesco, M., Camerlenghi, A., Volpi, V., Neagu, C., Accettella, D., Lindberg, B.,
693 Cova, A., Zgur, F., 2007. Interaction of processes and importance of contourites:
694 insights from the detailed morphology of sediment Drift 7, Antarctica.
695 Geological Society, London, Special Publications 276, 95-110.

696 Rebesco, M., Neagu, R.C., Cuppari, A., Muto, F., Accettella, D., Dominici, R., Cova,
697 A., Romano, C., Caburlotto, A. 2009. Morphobathymetric analysis and evidence
698 of submarine mass movements in the western Gulf of Taranto (Calabria margin,
699 Ionian Sea). *International Journal of Earth Sciences* 98, 791-805.

700 Reeder, D.B., Ma, B.B., Yang, Y.J., 2011. Very large subaqueous sand dunes on the
701 upper continental slope in the South China Sea generated by episodic, shoaling
702 deep-water internal solitary waves. *Marine Geology* 279, 12-18.

703 Ribó, M., Durán, R., Puig, P., Van Rooij, D., Guillén, J., Masqué, P., 2018. Large
704 sediment waves over the Gulf of Roses upper continental slope (NW
705 Mediterranean). *Marine Geology* 399, 84-96.

706 Ribó, M., Puig, P., Muñoz, A., Lo Iacono, C., Masqué, P., Palanques, A., Acosta, J.,

707 Guillén, J., Gómez Ballesteros, M., 2016. Morphobathymetric analysis of the
708 large fine-grained sediment waves over the Gulf of Valencia continental slope
709 (NW Mediterranean). *Geomorphology* 253, 22-37.

710 Ribbe, J., Holloway, P.E., 2001. A model of suspended sediment transport by internal
711 tides. *Continental Shelf Research* 21, 395-422.

712 Shepard, F.P., 1981. Submarine Canyons: Multiple Causes and Long-Time Persistence.
713 *Aapg Bulletin-American Association of Petroleum Geologists* 65, 1062-1077.

714 Shillington, D.J., Seeber, L., Sorlien, C.C., Steckler, M.S., Kurt, H., Dondurur, D.,
715 Cifci, G., Imren, C., Cormier, M.H., McHugh, C.M.G., Gurcay, S., Poyraz, D.,
716 Okay, S., Atgin, O., Diebold, J.B., 2012. Evidence for widespread creep on the
717 flanks of the Sea of Marmara transform basin from marine geophysical data.
718 *Geology* 40, 439-442.

719 Sultan, N., Cochonat, P., Canals, M., Cattaneo, A., Dennielou, B., Haflidason, H.,
720 Laberg, J.S., Long, D., Mienert, J., Trincardi, F., Urgeles, R., Vorren, T.O.,
721 Wilson, C., 2004. Triggering mechanisms of slope instability processes and
722 sediment failures on continental margins: a geotechnical approach. *Marine*
723 *Geology* 213, 291-321.

724 Sun, Q.L., Alves, T., Xie, X.N., He, J.X., Li, W., Ni, X.L., 2017. Free gas
725 accumulations in basal shear zones of mass-transport deposits (Pearl River
726 Mouth Basin, South China Sea): An important geohazard on continental slope
727 basins. *Marine and Petroleum Geology* 81, 17-32.

728 Sun, Q.L., Wu, S.G., Cartwright, J., Dong, D.D., 2012. Shallow gas and focused fluid

729 flow systems in the Pearl River Mouth Basin, northern South China Sea. *Marine*
730 *Geology* 315-318, 1-14.

731 Symons, W.O., Sumner, E.J., Talling, P.J., Cartigny, M.J.S., Clare, M.A., 2016.
732 Large-scale sediment waves and scours on the modern seafloor and their
733 implications for the prevalence of supercritical flows. *Marine Geology* 371,
734 130-148.

735 Talling, P.J., Allin, J., Armitage, D.A., Arnott, R.W.C., Cartigny, M.J.B., Clare, M.A.,
736 Felletti, F., Covault, J.A., Girardclos, S., Hansen, E., Hill, P.R., Hiscott, R.N.,
737 Hogg, A.J., Clarke, J.H., Jobe, Z.R., Malgesini, G., Mozzato, A., Naruse, H.,
738 Parkinson, S., Peel, F.J., Piper, D.J.W., Pope, E., Postma, G., Rowley, P.,
739 Sguazzini, A., Stevenson, C.J., Sumner, E.J., Sylvester, Z., Watts, C., Xu, J.,
740 2015. Key future directions for research on turbidity currents and their deposits.
741 *Journal of Sedimentary Research* 85, 153-169.

742 Taylor, B., Hayes, D.E., 1980. The tectonic evolution of the South China Basin. In:
743 Hayes, D.E. (Ed.) *The Tectonic and Geologic Evolution of Southeast Asian Seas*
744 *and Islands*, Am. Geophys. Union Monogr. 23, 89-104.

745 Urlaub, M., Geersen, J., Krastel, S., Schwenk, T., 2018. Diatom ooze: Crucial for the
746 generation of submarine mega-slides? *Geology* 46, 331-334.

747 Wynn, R.B., Stow, D.A.V., 2002. Classification and characterisation of deep-water
748 sediment waves. *Marine Geology* 192, 7-22.

749 Wynn, R.B., Weaver, P.P.E., Ercilla, G., Stow, D.A.V., Masson, D.G., 2000.
750 Sedimentary processes in the Selvage sediment-wave field, NE Atlantic: new

751 insights into the formation of sediment waves by turbidity currents.
752 *Sedimentology* 47, 1181-1197.

753 Xie, X.N., Müller, R.D., Li, S., Gong, Z.S., Steinberger, B., 2006. Origin of
754 anomalous subsidence along the Northern South China Sea margin and its
755 relationship to dynamic topography. *Marine and Petroleum Geology* 23,
756 745-765.

757 Yang, Q.X., Tian, J.W., Zhao, W., 2010. Observation of Luzon Strait transport in
758 summer 2007. *Deep Sea Research Part I: Oceanographic Research Papers* 57,
759 670-676.

760 Zhao, Y.L., Liu, Z.F., Zhang, Y.W., Li, J.R., Wang, M., Wang, W.G., Xu, J.P., 2015. In
761 situ observation of contour currents in the northern South China Sea:
762 Applications for deepwater sediment transport. *Earth and Planetary Science*
763 *Letters* 430, 477-485.

764 Zhao, Z.X., Klemas, V., Zheng, Q.N., Yan, X.H., 2004. Remote sensing evidence for
765 baroclinic tide origin of internal solitary waves in the northeastern South China
766 Sea. *Geophysical Research Letters* 31.

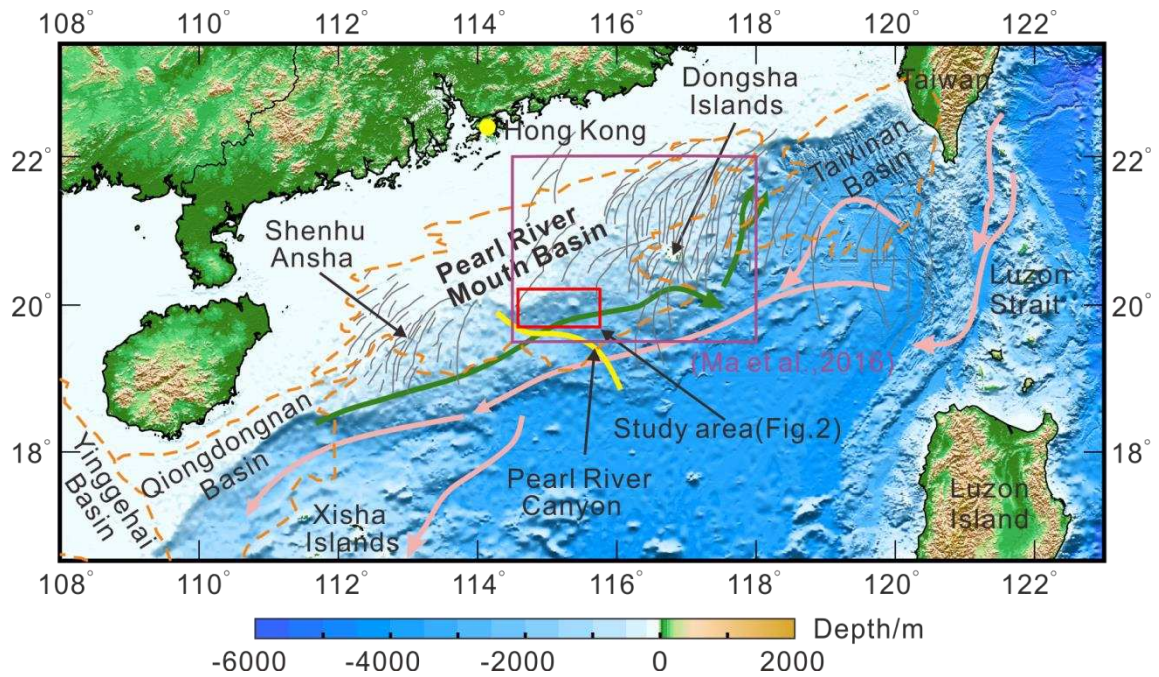
767 Zhu, M.Z., Graham, S., Pang, X., McHargue, T., 2010. Characteristics of migrating
768 submarine canyons from the middle Miocene to present: Implications for
769 paleoceanographic circulation, northern South China Sea. *Marine and Petroleum*
770 *Geology* 27, 307-319.

771 Zhu, W.L., Huang, B.J., Mi, L.J., Wilkins, R.W.T., Fu, N., Xiao, X.M., 2009.
772 Geochemistry, origin, and deep-water exploration potential of natural gases in

773 the Pearl River Mouth and Qiongdongnan basins, South China Sea. Aapg
774 Bulletin 93, 741-761.
775
776

777 **Figures and Figure Captions**

778



779

780 Fig.1 Bathymetric map of the northern South China Sea margin. The orange dashed

781 lines highlight the distribution of four major deep-water sedimentary basins. The

782 yellow curve represents the location of the Pearl River Canyon. The grey curves

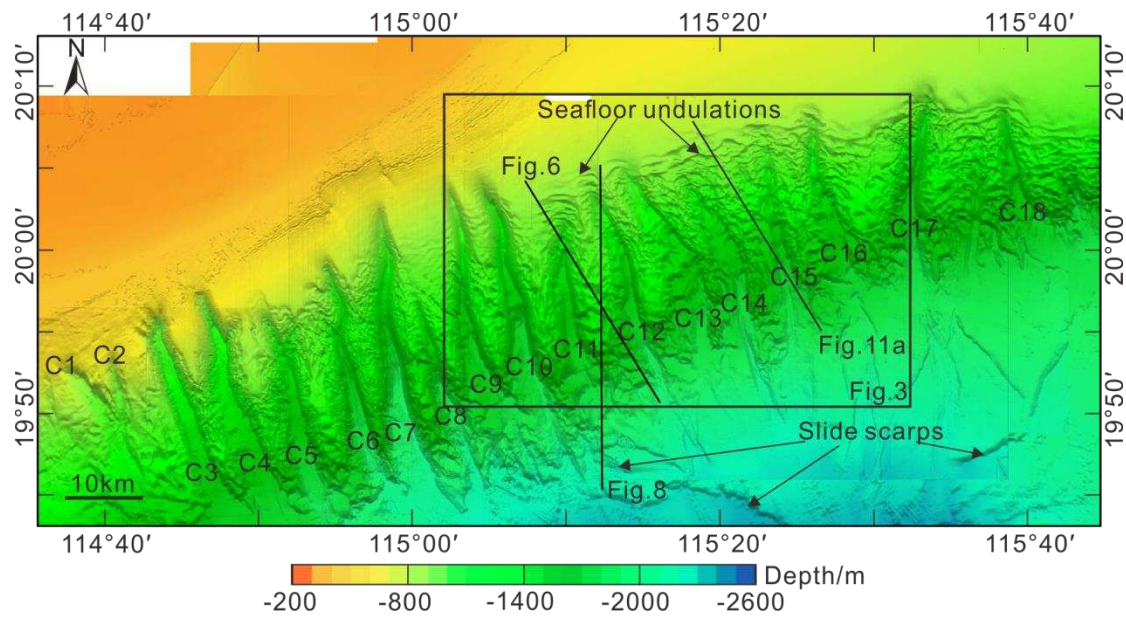
783 represent internal waves observed in satellite imagery (extracted from Zhao et al.,

784 2004; Li et al., 2011). The red box outlines the area enlarged in Figure 2. The purple

785 box represents extent of internal waves and the region of *in situ* current measurements

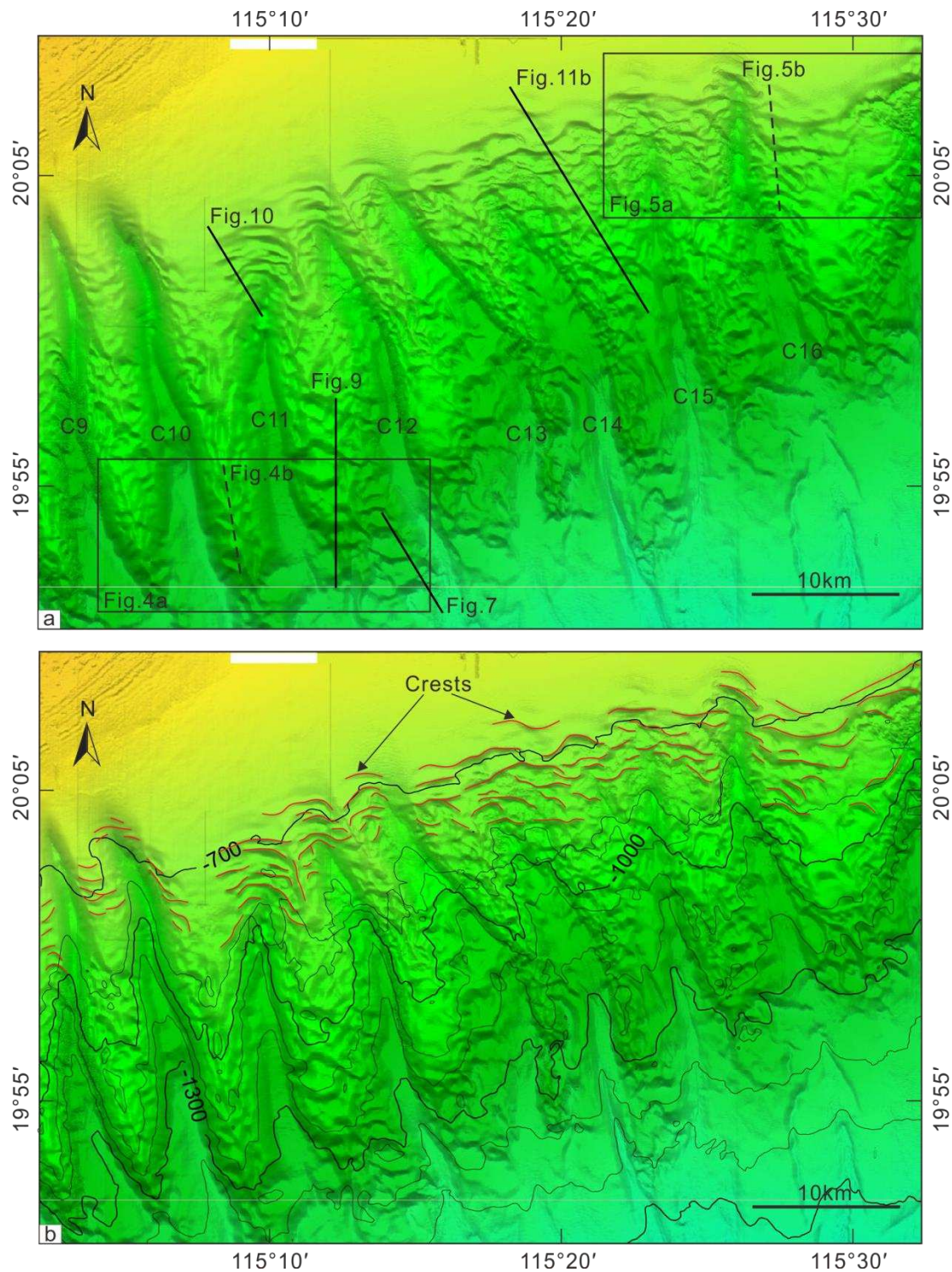
786 (Ma et al., 2016). The green and pink arrows indicate the circulation pathways of

787 intermediate and deep-water masses, respectively (modified after Chen et al., 2014).



788

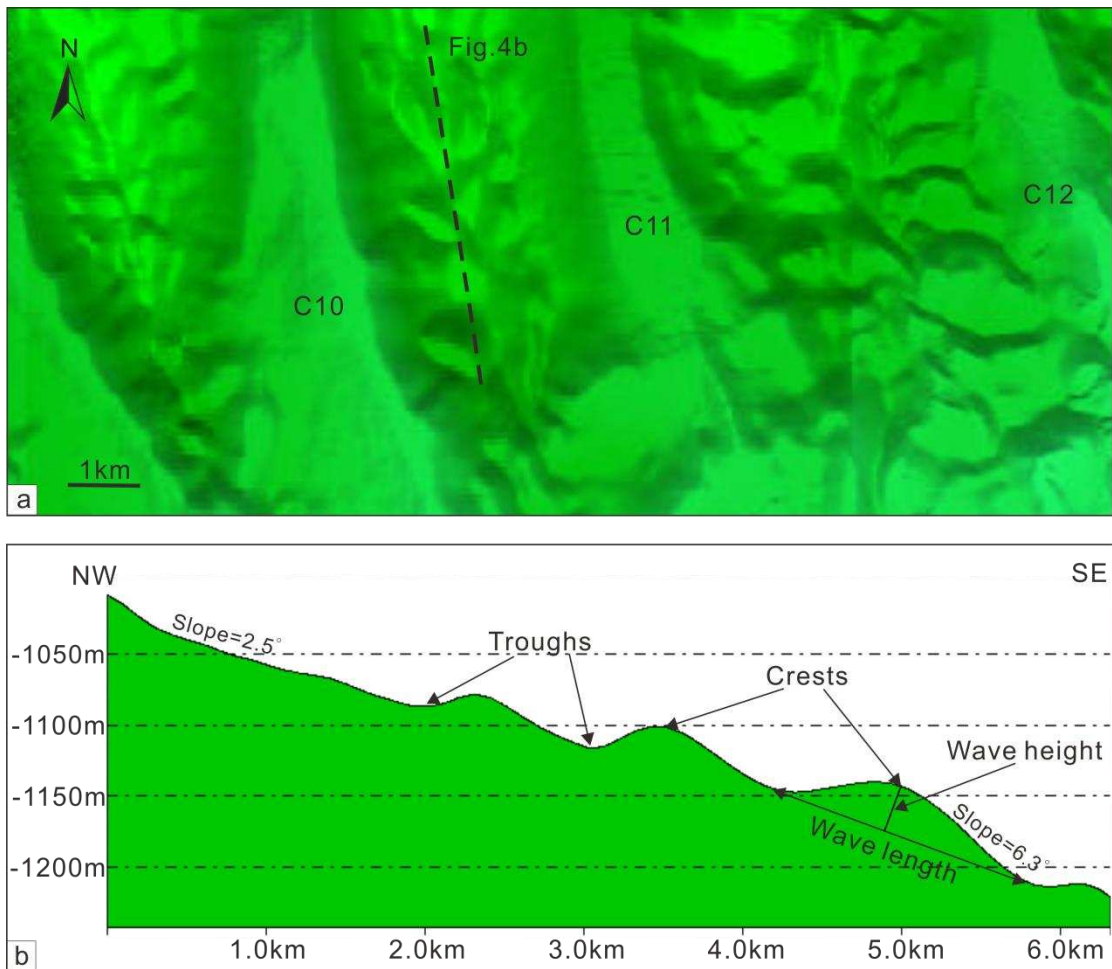
789 Fig. 2 High-resolution bathymetric map of the study area showing eighteen submarine
 790 canyons (C1 to C18) with a NW-SE orientation. Note that the heads of C9 to C18
 791 show widespread sea floor undulations. Several slide scarps are clearly identified
 792 downslope from the submarine canyons. The black box represents the location of
 793 Figure 3. The black lines show the location of the high-resolution seismic profiles in
 794 Figures 6, 8 and 11.



795

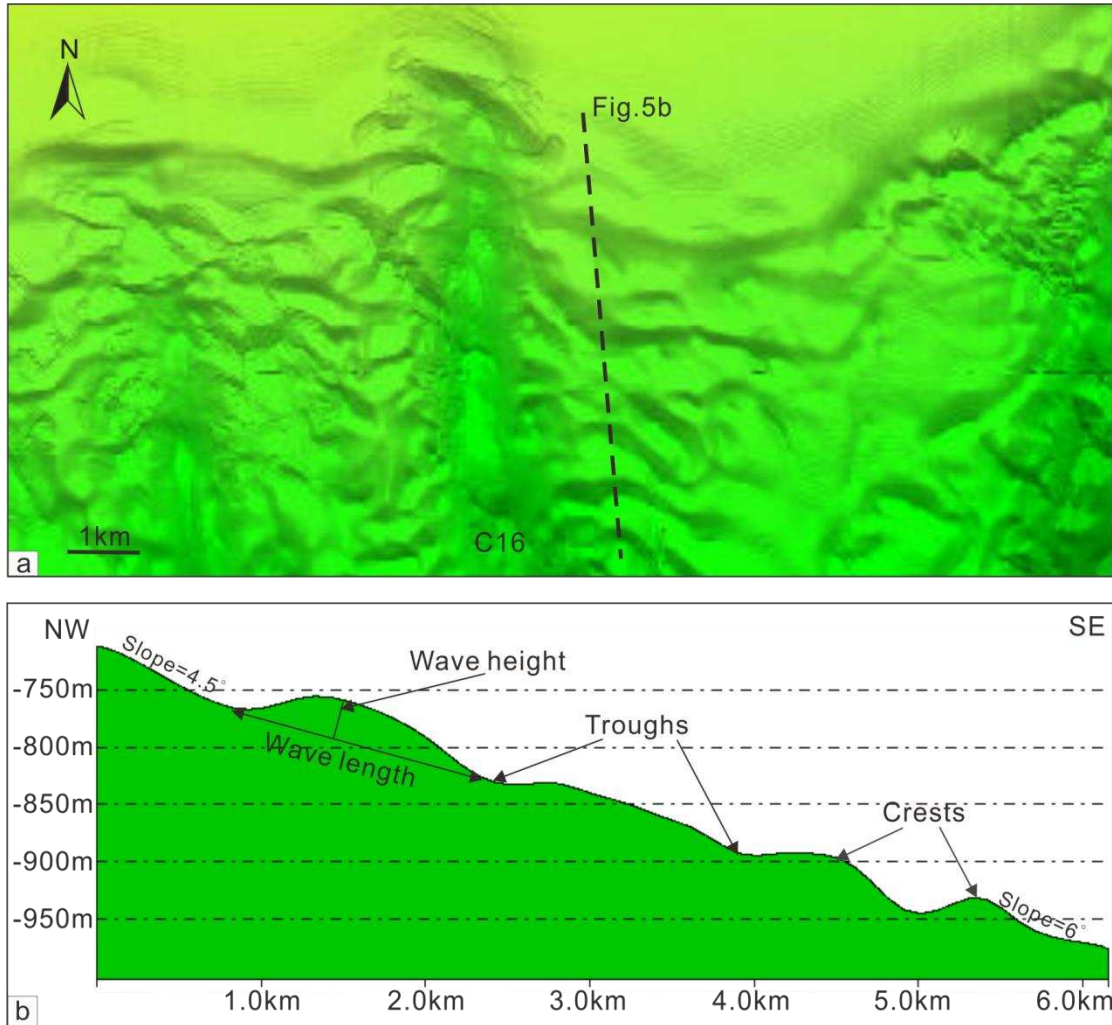
796 Fig. 3 (a) Bathymetric map illustrating the detailed morphology of the studied
 797 seafloor undulations. Seafloor undulations are mainly located at the heads and flanks
 798 of the submarine canyons. The black solid lines represent the locations of the 2D
 799 seismic profiles used in this study. The black dotted lines indicate the locations of

800 bathymetric profiles show in Figs. 4b and 5b. (b) Distribution of the crests of seafloor
 801 undulations on the bathymetric map. The crests of the seafloor undulations are show
 802 in red and are parallel or sub-parallel to the bathymetric contours. The contour
 803 interval is 100 m.
 804



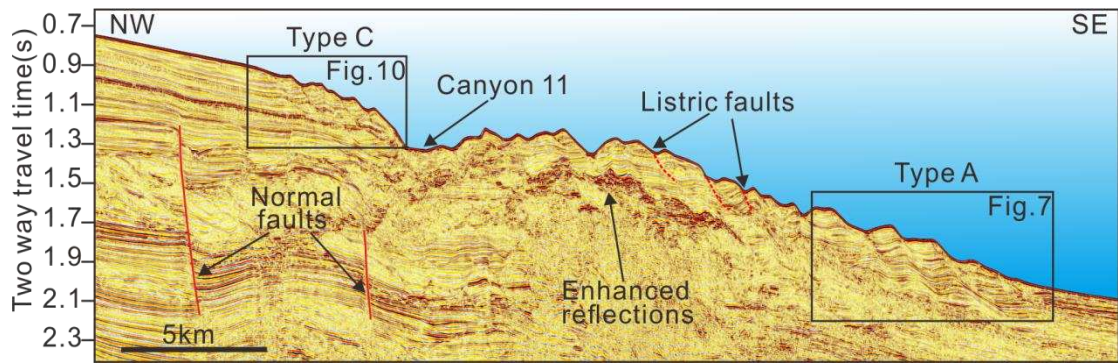
805
 806 Fig. 4 (a) Bathymetric map revealing the detailed seafloor morphology of the lower
 807 flanks of submarine canyons, stressing the presence of widely distributed seafloor
 808 undulations. See Fig. 3 for the location of the bathymetric survey. (b) Bathymetric
 809 profile crossing the flank area between Canyon 10 and 11 and revealing multiple
 810 seafloor undulations. The wavelength and height of these seafloor undulations can

811 reach up to 2 km and 100 m, respectively.



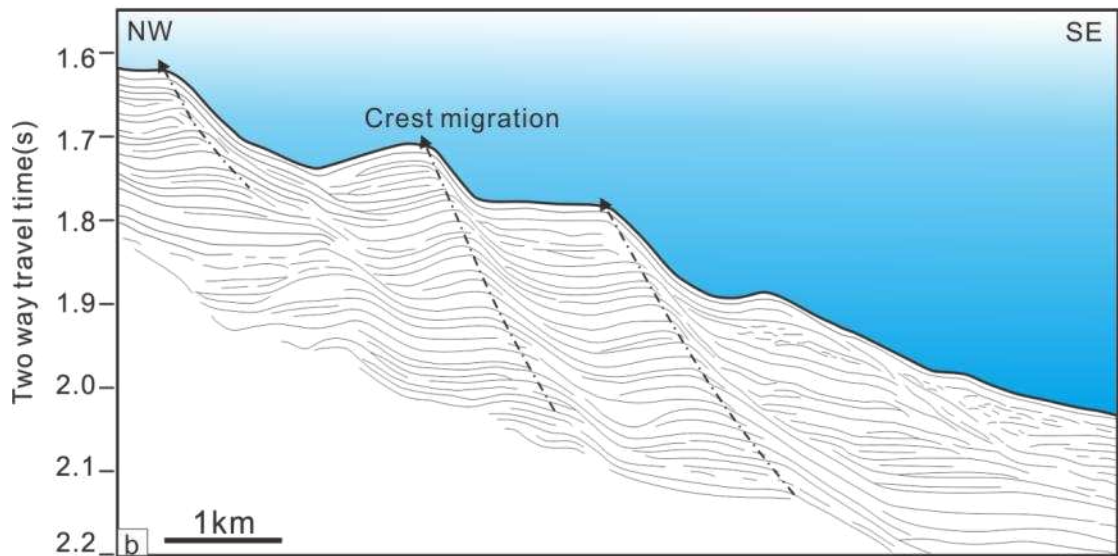
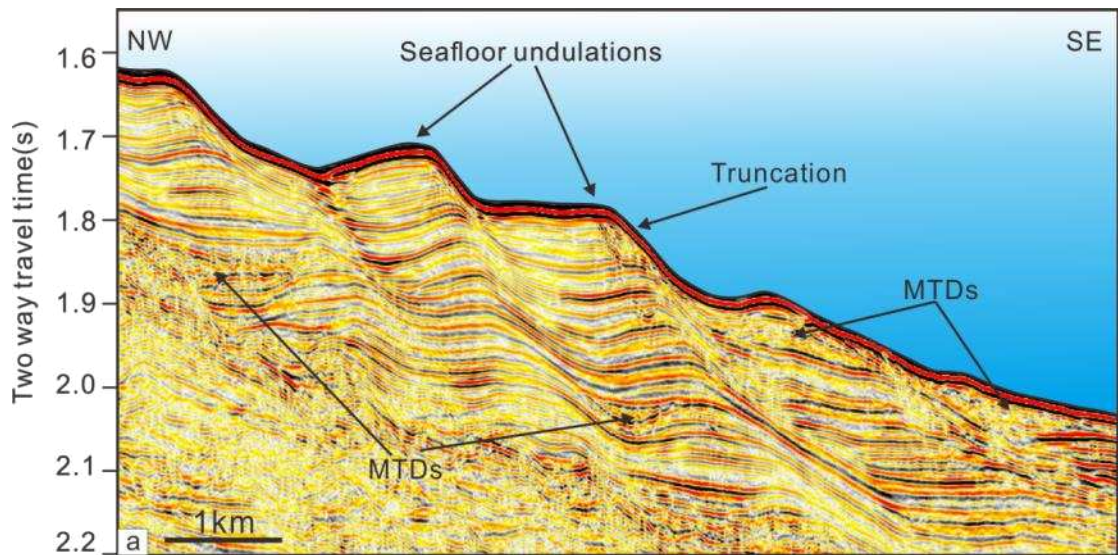
812
813 Fig. 5 (a) Bathymetric map highlighting the detailed seafloor morphology of the upper
814 continental slope. Widespread seafloor undulations can be observed. See Fig. 3 for the
815 location of the bathymetric survey. (b) Bathymetric profile crossing the upper ridge
816 area between canyon 16 and 17, revealing the presence of multiple seafloor
817 undulations. They can be up to 1.5 km in wavelength (trough to trough) and 50 m in
818 height (maximum relief).

819



820

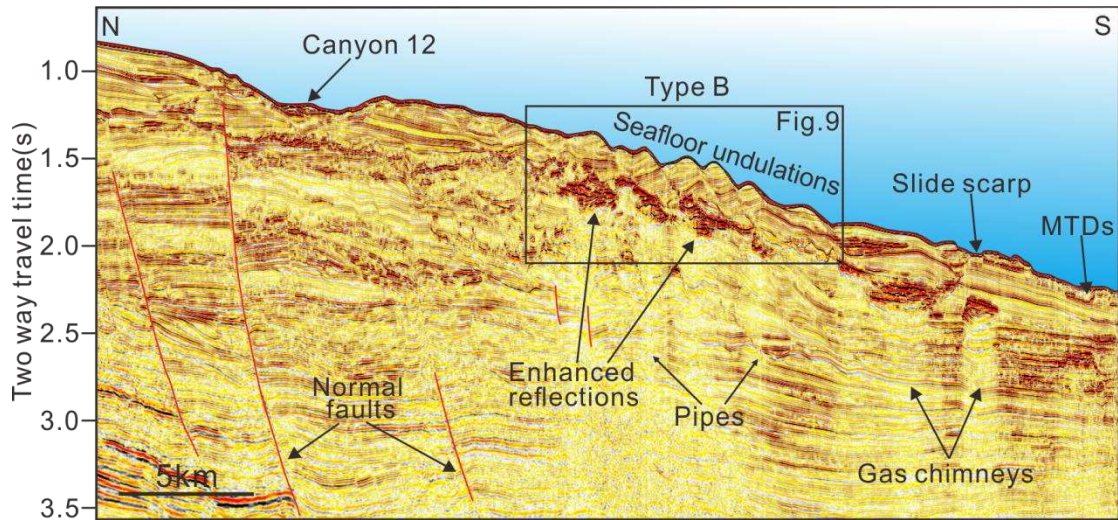
821 Fig. 6 Two-dimensional (2D) seismic line crossing the head of Canyon 11 and the
 822 flank area between C11 and C12 (for location of the profile see Fig. 2). Several
 823 large-scale normal faults and listric faults can be distinguished, which are marked by
 824 red solid and dotted lines, respectively. Note the presence of high-amplitude enhanced
 825 seismic reflections beneath some of the seafloor undulations.



826

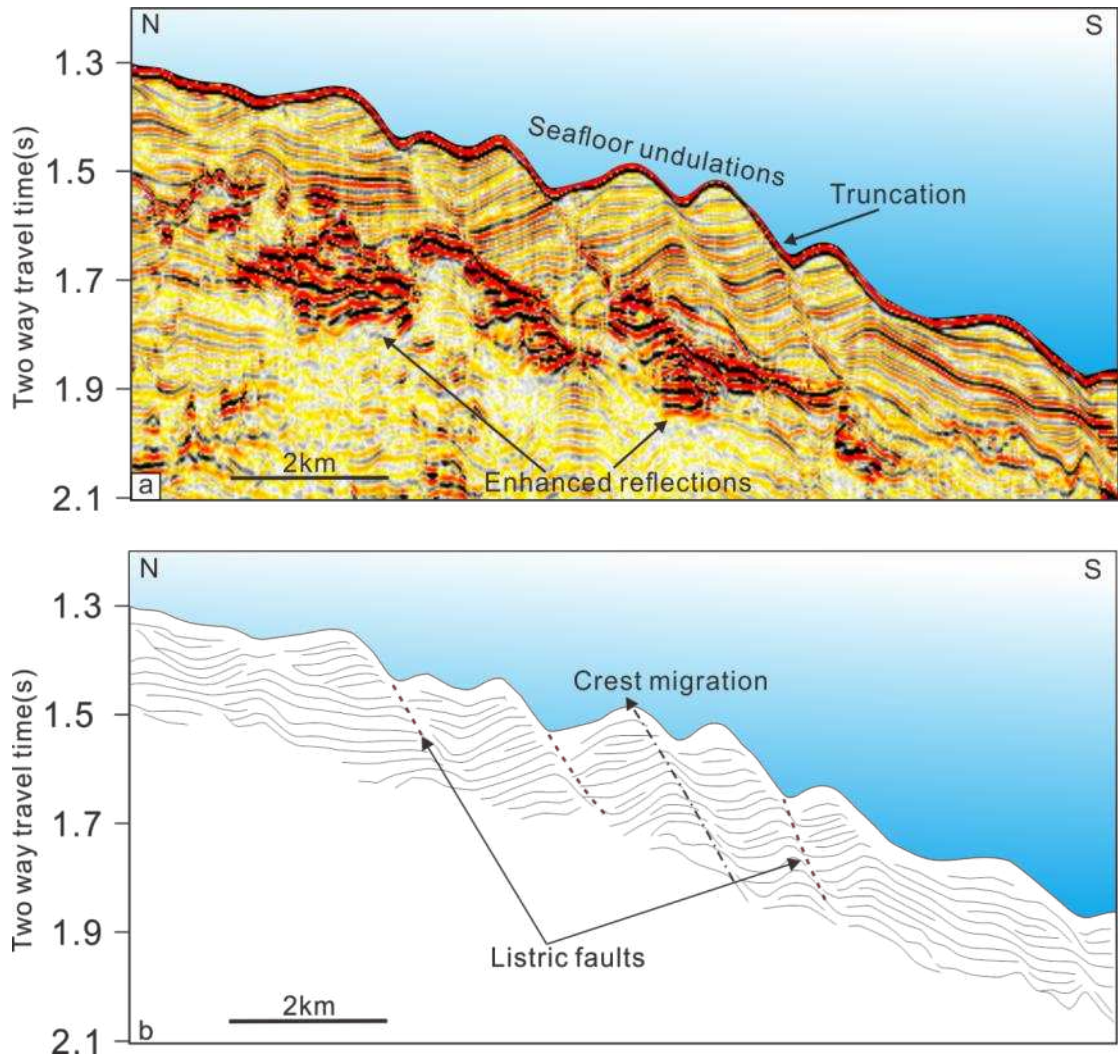
827 Fig. 7 (a) Zoomed section of the seismic profile in Fig. 6 revealing the detailed
 828 internal character of the seafloor undulations in the lower reach of the canyon flanks,
 829 between C11 and C12. Seafloor undulations are clearly observed on the seafloor and
 830 their crests show an upslope migration trend. Note that the downslope flanks of most
 831 of the undulated structures are steeper than their upslope counterparts. Several MTDs
 832 can be distinguished within the seafloor undulations. (b) Line-drawn interpretation of
 833 Fig. 7a revealing the internal seismic reflectors within the undulations, which are
 834 continuous across the troughs separating distinct undulations.

835



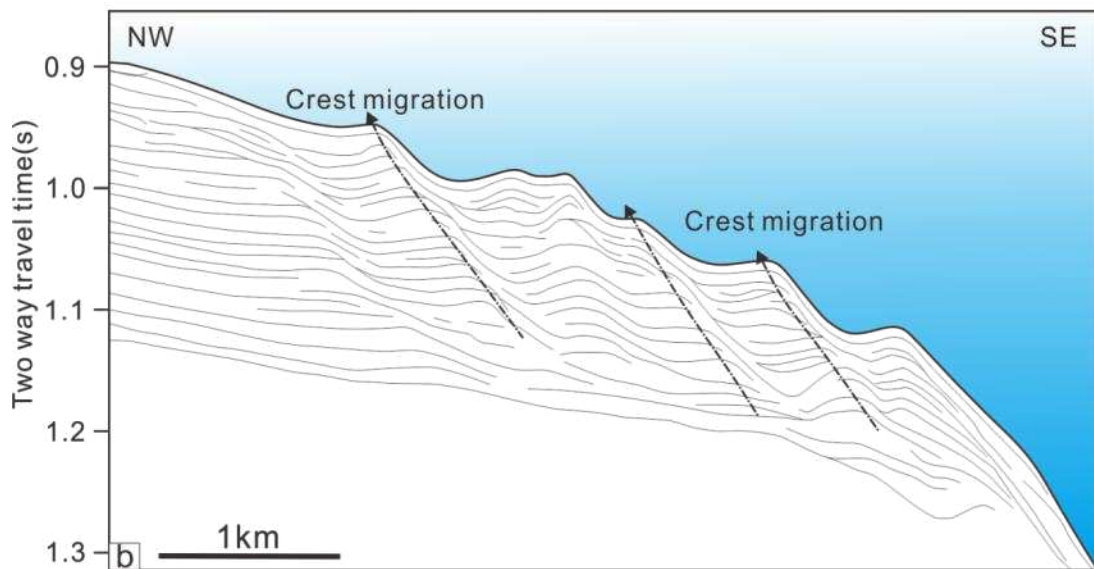
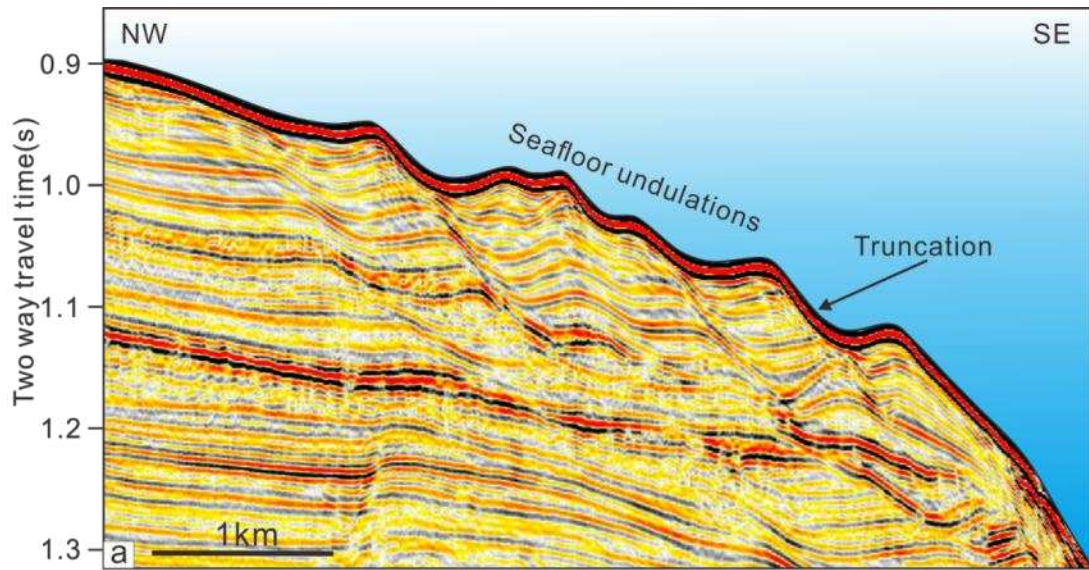
836

837 Fig. 8 High-resolution seismic profile crossing C12 and the canyon flank between
838 C11 and C12 (for location of the profile see Fig. 2). A slide scarp and multiple
839 seafloor undulations can be identified on the modern seafloor. Note the presence of
840 gas chimneys, pipes and high-amplitude (enhanced) seismic reflections beneath the
841 undulations.



842

843 Fig. 9 (a) Zoomed section of the seismic profile in Fig. 8 showing the internal
 844 architecture of seafloor undulations on the canyon flank between C11 and C12.
 845 Seismic reflections within seafloor undulations are not continuous and cannot be
 846 traced across the troughs from one wave to the next. Most of the seafloor undulations
 847 are separated by small-scale listric faults. (b) Line-drawn interpretation of Fig. 9a
 848 illustrating the internal seismic reflections within the seafloor undulations, which are
 849 not continuous.



850

851 Fig.10 (a) Zoomed section of the seismic profile in Fig. 6 showing the detailed

852 internal architecture of sediment waves at the head of C11. Internal seismic reflections

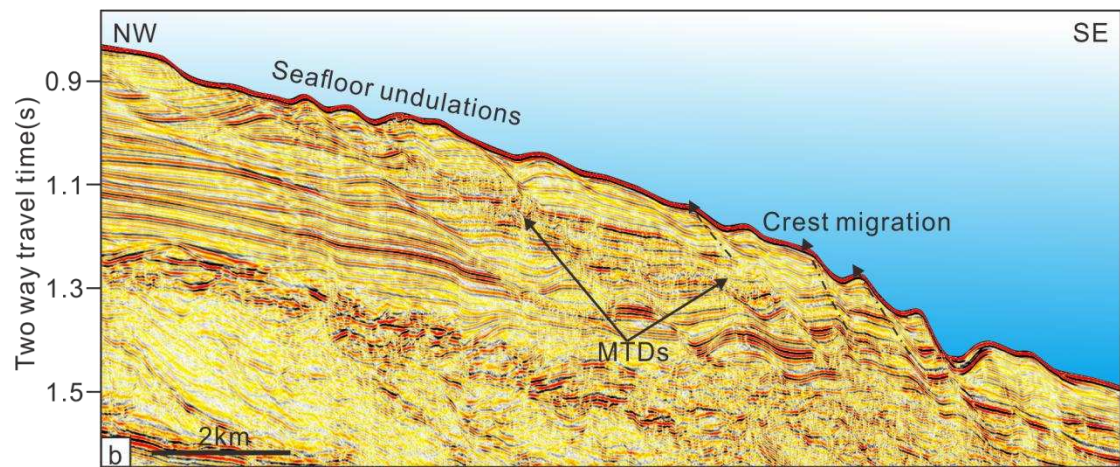
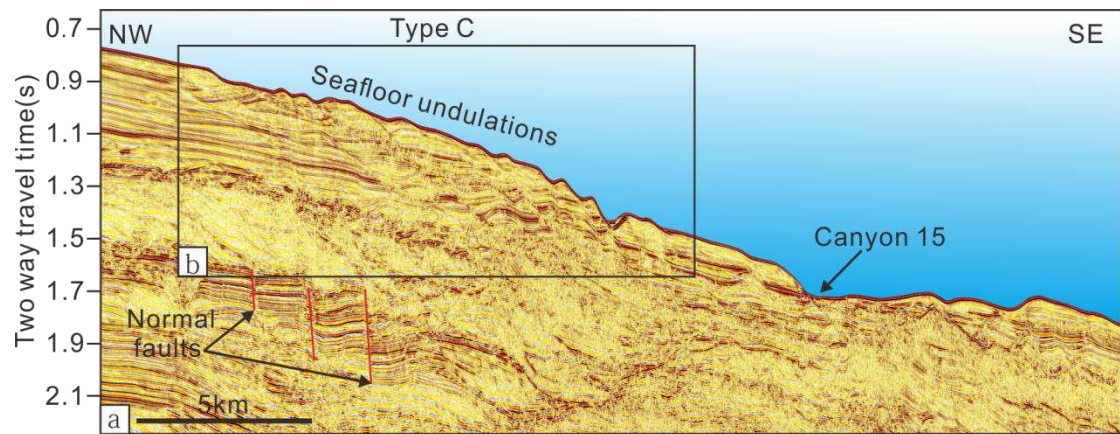
853 within the seafloor undulations are continuous and can be traced from one wave to the

854 next. Note that the crests of the undulated structures reveal an upslope migration

855 pattern. (b) Line-drawn interpretation of Fig. 10a highlighting that most of the internal

856 reflectors crossing the different seafloor undulations are continuous.

857



858

859 Fig. 11 (a) Two-dimensional (2D) seismic profile crossing C15 and the canyon flank

860 between C14 and C15 (see Fig. 2 for location of the profile). Multiple sediment waves

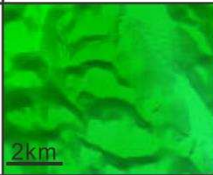
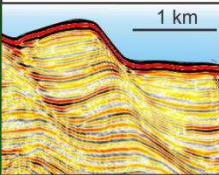
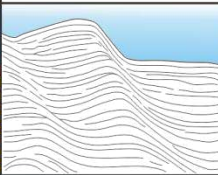
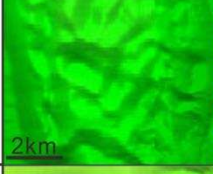
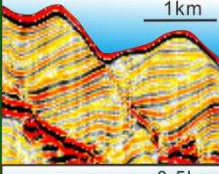
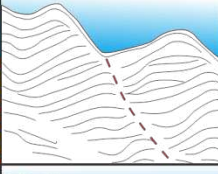
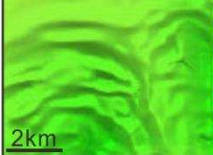
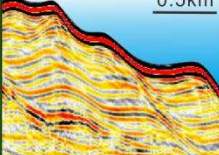
861 are observed in the canyon head. (b) Zoomed section in Fig. 11b showing the internal

862 architecture of sediment waves in the canyon head. Note that most of the sediment

863 waves show an upslope migration trend. Several MTDs can be identified within the

864 imaged sediment waves.

865

Types	Locations	Seafloor morphology	Seismic characteristics	Line drawing	Wave-forming process
Type A	Lower of canyon thalwegs				Turbidity currents
Type B	Canyon flanks				Submarine creeps
Type C	Canyon heads				Internal waves

866

867 Fig. 12 Classification of three different types of seafloor undulations based on their
868 location and origin. Representative seismic profiles and related line drawings
869 illustrate the formation mechanisms of the seafloor undulations. Types A and B
870 undulations are distributed in the canyon areas. The former are generated by turbidity
871 currents, while the latter are generated by gravitational deformation processes
872 (gravity-driven submarine creep). Type C undulations are mainly located at the heads
873 of the submarine canyons and were generated by internal waves.